BLDC Motor and Drive Low Frequency Conducted RFI Simulation for Automotive Applications

J. E. Makaran

Siemens VDO Automotive Inc. 1020 Adelaide St. S., London, Ontario, N6E 1R6

J. LoVetri

Department of Electrical and Computer Engineering, The University of Manitoba, Winnipeg, Manitoba, R3T 5V6

Abstract

In considering automotive conducted RFI specifications applicable to motors and their associated drives, simulation of conducted radio frequency emissions in the range from 150 kHz to 1 MHz is an area of interest from the product design perspective for several reasons. Traditionally, suppression of conducted noise in this frequency range of interest has been achieved through the use of bulk capacitance. These capacitors not only limit the lifetime of the motor, but they also consume valuable space within the motor, as well as add cost motor. The selection of bulk noise suppression elements has in the past been predominately made through trial and error "brute force" methods. The following paper presents a method whereby low frequency conducted RFI emissions can be simulated through the use of a high fidelity virtual motor and drive model, as well as a virtual spectrum analyzer.

Introduction

In recent years, brushless DC (BLDC) motors have been introduced for engine cooling applications, replacing conventional belt driven and electrodrive cooling fans with one or two discrete speeds. In automobiles, the introduction of electronically commutated motors has been accompanied by a proliferation of electronic devices. With this proliferation of electronic devices, an emphasis has been placed on EMC issues. In recent years, there has been an increase in the capabilities of electronic simulation tools, the result being the feasibility of creating simulation models of complete electromechanical systems. Through the use of analog behavioral modeling, the mechanical behaviour of the motor and its associated load can be created through the use of an electronics simulation package such as PSPICE®. Such a model can be used not only to predict low frequency phenomenon such as torque ripple, but can also be extended to the prediction of conducted RFI

emissions. The virtual motor model proposed in this study includes measured, lumped parameter models of the self inductance of the motor phases, as well as mutual coupling between the motor phases, iron losses, as well as the associated pulse width modulated (PWM) drive and load.

Two separate motor windings were studied. The first winding was a 10 turn, 17 AWG. The second winding was a 9 turn, 18 AWG winding.

Several pertinent papers have been published in recent years concerning the simulation of conducted RFI emissions in brushless motors [1-6] for industrial applications. All of these publications pertain to applications concerning conducted emissions for high voltage, three phase, asynchronous, bipolar motors for electric vehicles used in industrial applications. As such, there are no papers examining conducted RFI emissions from low voltage, high current, unipolar permanent magnet motors. This paper considers the simulation of conducted RFI emissions from a 13 V, 400W, five phase, permanent magnet, unipolar, brushless DC motor for use in an underhood automotive engine cooling application. The frequency range of interest for this study ranges from 0.15 to 1 MHz.

Model Formulation

A block diagram of the system that was modeled is depicted in Figure 1.
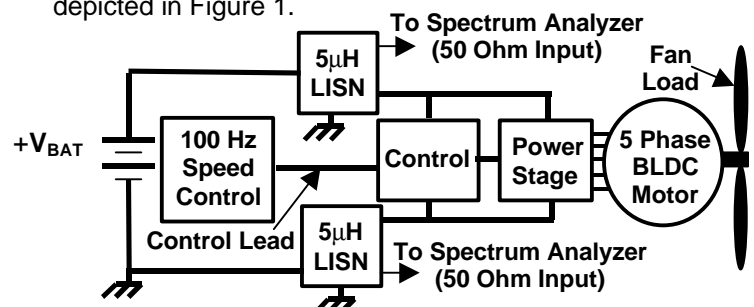

Figure 1. Schematic representation of system model.

The magnitude of conducted RFI emissions in motors and drives is dominated by the magnitude and switching times of the motor current. As such, the formulation of the system model examining the interaction between electrical, magnetic, and mechanical behavior of the motor and load can be considered. This relationship is represented in block form in Figure 2.
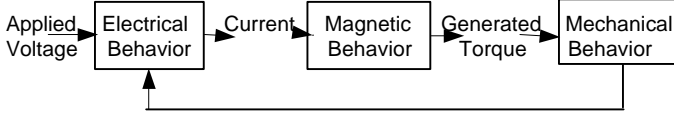

Figure 2. Relationship between electrical, magnetic, and mechanical system behavior.

The electrical behavior of the machine is described by:

$$v = r^T i + d/dt\,[L(q_r)\,i] + d/dt\,l_m(q_r) \tag{1}$$

Where the applied voltage vector, v, represents the voltage applied to the terminals of the motor (V). In the case where pulse width modulation (PWM) is used to control the speed of the motor, v will be a function of the PWM duty cycle. At full speed, the motor terminals will see the full battery voltage (PWM duty cycle = 100%). The vector r represents the DC resistance vector of the motor phases (Ω). The rotor position is represented by θ_r (rad). $L(q_r)$ is the motor inductance matrix as a function of rotor position (H). The inductance matrix will include self and mutual inductance terms. $l_m(q_r)$ is the airgap magnetic flux as a function of rotor position (Wb). The phase current vector is represented by i (A).

The magnetic behavior of the machine is governed by:

$$dq_r/dt\; T_e = [\,i^T\; d/dt\,l_m(q_r)] \tag{2}$$

where the generated electromagnetic torque is represented by T_e (Nm).

The mechanical behavior of the machine is governed by:

$$T_e = J\,d^2q_r/dt^2 + B_m\;dq_r/dt + T_L \tag{3}$$

Where J is the moment of inertia of the motor rotor and fan load (kg m^2), B_m represents the iron and damping losses of the motor (Nm s/ rad), and T_L represents the motor load (Nm). For the case of a fan load:

$$T_L = (dq_r/dt)^2 / K_{fan}^2 \tag{4}$$

Where the motor shaft speed is represented by dq_r/dt (rad s^{-1}) and K_{fan} is the fan load constant (rad s^{-1}/Nm $^{1/2}$).

If the characterization of low frequency motor performance is desired, solving equations (1) – (3) can be performed through numerical means. A numerical approach to solving the equations has been used in the past to model low-frequency behavior of motors and their associated loads. The equations governing the behavior of a three phase synchronous machine under no-load conditions have been solved using the Runge-

Kutta technique [7]. In a similar manner, real time simulation of induction motors has been performed. Authors such as Strahan [8], Zhang et al: [8], Jack et al: [9-10] and Cho [11], to name a few, have created motor models based on numerical solutions to differential equations for the study of motor performance. Typically, models based on the solution of the aforementioned equations can be used to evaluate general electromagnetic behaviour but RFI concerns are not taken into account. This is due primarily to the difficulty of solving equations incorporating parasitic properties associated with circuit elements.

A survey of literature dealing with brushless applications has shown that work in the prediction of conducted RFI emissions has been limited to motors and drives for high voltage, three phase bipolar induction motors. As such, there are no papers examining conducted RFI emissions from low voltage, high current, permanent magnet motors for automotive applications. In the prediction of conducted RFI emissions, steady state system behavior under mid speed and high speed conditions is of concern.

To attempt to model the high frequency behavior of the machine, drive, and associated load, a numerical solution based on modifying the above equations is impractical. The primary reason is the high number of energy storage elements (capacitors and inductors) that are present in the motor and drive. These elements would add to the complexity of the set of differential equations. To predict the conducted RFI behavior of the system in the frequency range of interest, bulk and parasitic elements of active and passive components in the inverter must be included. In order to include parasitic terms present in electronic components such as diodes and MOSFETs, the entire motor and drive system was simulated using lumped element modeling in PSPICE^{TM}.

The SPICE Electrical Motor Model

The magnetic behavior of the machine and the fan load were determined experimentally and incorporated in the model. As such, the magnetic model employed was a lumped, measured parameter model. All magnetic parameters such as back EMF constants, self and mutual inductances were measured. The complete model of one motor phase is shown in Figure 3. In this figure, the top of the motor phase is connected to the positive voltage supply. This connection in turn, is in series with a current controlled voltage source which is used as the phase current observer. This is in series with the phase back EMF, the phase self-inductance, and the phase winding resistance. The trapezoidal motor phase back EMF was modeled as a voltage source. At the bottom of the motor phase is a voltage source used to represent the sum of the mutually coupled voltages from the other motor phases. The individual mutually coupled voltage contributions incorporate the actual measured values of the mutual inductance between the phase of interest and the other motor phases. A description of the dependent voltage sources used to model mutual coupling occurs later in this section.

In parallel with the motor phase were the phase self-capacitance, and the phase iron losses obtained through motor loss separation tests.
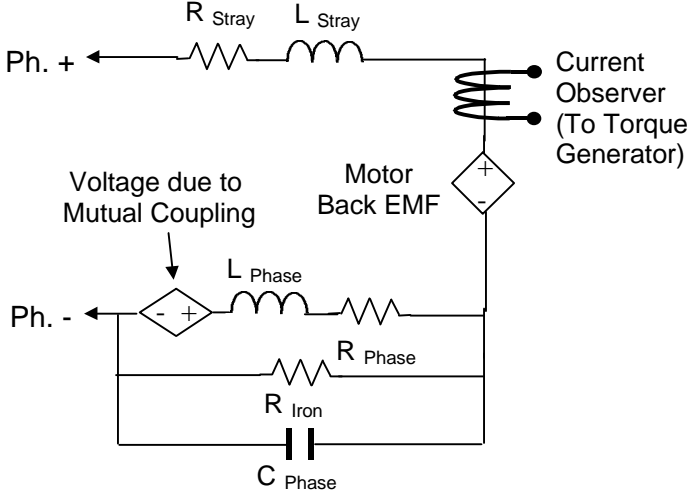

Figure 3. Electrical model of a single motor phase

In a PWM motor drive, conducted RFI emissions at lower frequencies are influenced by the larger energy storage elements in the motor and drive, such as the motor phase inductance. As such, it was decided to measure the motor self and mutual inductances as a function of rotor position using a similar coil excitation as would be experienced in the application. Consequently, measuring the coil inductance using an LCR meter was ruled out. To obtain a method that would take into account the magnetic behaviour of the motor under various operating conditions, the following relationship was examined. By definition, an inductance *L*, for any angular position, θ, can be defined as;

$$L(\boldsymbol{q}_r) = \boldsymbol{l}(\boldsymbol{q}_r) / i \quad \text{(H)} \qquad (5)$$

Where, $\boldsymbol{l}(\boldsymbol{q}_r)$ is the total flux produced in the inductance linking that phase for the angular position of interest (Wb), and *i* is the current in the inductance (A). The induced EMF in the inductance may be defined as:

$$E(\boldsymbol{q}_r) = -N \, d\boldsymbol{f}(\boldsymbol{q}_r) / dt \quad \text{(V)} \qquad (6)$$

By integrating the induced EMF with respect to time, the total flux linkage $\lambda(\theta_r)$ may be obtained:

$$\boldsymbol{l}(\boldsymbol{q}_r) = \int_0^t E(\theta_r) \, dt \quad \text{(Wb)} \qquad (7)$$

Once the total flux was determined, the inductance of the motor phase was obtained. In our measurements, excitation of the motor phase to a desired magnitude of current was achieved through low frequency switching of the motor phase (~0.5 Hz), and subsequent integration of the resultant EMF. The magnetic coupling between adjacent motor phases is analogous to the coupling present between the primary and secondary windings of a transformer. As such, the mutual coupling between

adjacent motor phases was determined through the same method. This arrangement is outlined in Figure 4. As may be seen, there are two separate integrators, one to determine the primary motor phase inductance, and one to determine the mutual coupling between a phase inductance and adjacent motor phase.

In performing the measurements, it was found that there was no significant variance in the self inductances of the motor phases. As such, these were represented by a single values independent of rotor position. The mutual inductances, however, were represented as functions of rotor position.
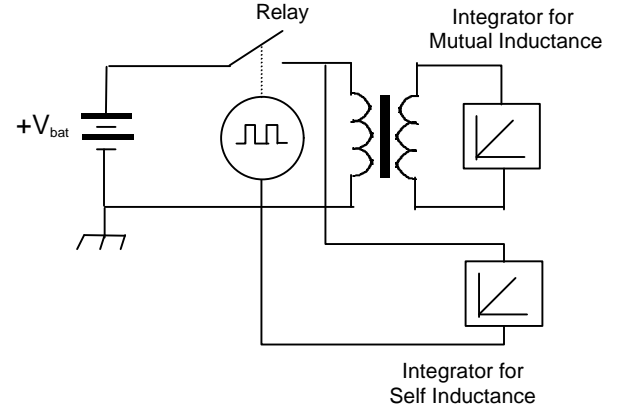

Figure 4. Experimental setup to determine motor inductance matrix

In considering the inclusion of mutual coupling terms in the PSPICE® model for a five-phase motor, the mutual coupling, or transformer action, between phases was modeled using dependent sources. Consider a simple transformer comprised of a primary and secondary winding as illustrated in Figure 5. The primary and secondary windings, L_1, and L_2 respectively, are assumed to be ideal and lossless. They are coupled together on a lossless iron core through a mutual inductance, *M*. The primary winding is connected to a voltage source. The voltage across the secondary of the transformer is represented as *Vs*.
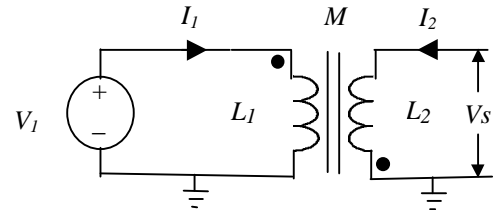

Figure 5. Simple transformer model used in modeling of mutual coupling between motor phases

Applying KVL to the voltage drops clockwise around the primary loop we have

$$L_1 \, dI_1 / dt - M \, dI_2 / dt = V_1 \qquad (8)$$

whereas in the secondary loop, going counter-clockwise, we have

$$L_2 \, dI_2 / dt - M \, dI_1 / dt = Vs \qquad (9)$$

We can think of the two terms $-M(dI_1/dt)$ and $-M(dI_1/dt)$ as voltage source contributions from the opposite side of the transformer. These two equations can be manipulated to get

$$L_1\, dI_1/dt - (M/L_2)[\,Vs + M\, dI_1/dt\,]$$

$$= L_1\, dI_1/dt - (M/L_2)\,Vs - (M^2/L_2)\, dI_1/dt = V_1 \qquad (10)$$

$$L_2\, dI_2/dt - (M/L_1)[\,V_1 + M\, dI_2/dt\,]$$

$$= L_2\, dI_2/dt - (M/L_1)\,V_1 - (M^2/L_1)\, dI_2/dt = V_s \qquad (11)$$

Writing the effective inductances as

$$L_1' = L_1 - (M^2/L_2)\ \text{and}\ L_2' = L_2 - (M^2/L_1) \qquad (12)$$

It is a simple matter to write the KVL equations as

$$L_1'\, dI_1/dt - (M/L_2)\,Vs = V_1 \qquad (13)$$

$$L_2'\, dI_2/dt - (M/L_1)\,V_1 = Vs \qquad (14)$$

When the mutual coupling between the windings is weak, the coupling factor M is small, so the M^2 term is negligible and $L_1' = L_1$ and $L_2' = L_2$. Our exact (or approximate) transformer equations can now be implemented as dependent voltage controlled voltage sources as shown in Figure 6.
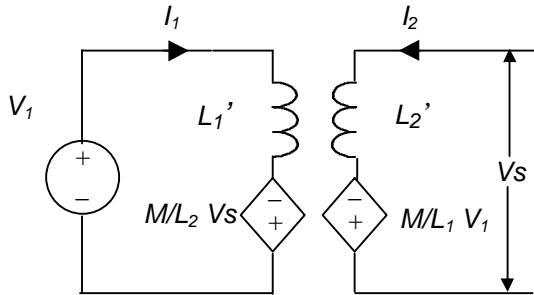

Figure 6. Transformer model showing mutually coupled voltage terms as dependent voltage terms

By knowing the value of the mutual inductance as a function of rotor position, the voltage drop across the primary inductance, and the primary inductance as a function of rotor position, the mutual coupling between two motor phases can be modeled as a dependent voltage source.

The SPICE Electromechanical Motor Model

In modeling the electromechanical motor model, the relationships in equations (2), (3) and (4) had to be considered and incorporated into the SPICE model as a circuit element. Fundamentally, this was an exercise of modeling the various electromechanical torques as circuit elements.

Considering the first term of the right hand side of equation (3) dealing with the torque contribution from the moment of inertia of the motor and fan we write

or

$$T_{Inertia} = J\, d^2q_r/dt^2 \qquad (15)$$

$$T_{Inertia} = J\, dw_r/dt \qquad (16)$$

where w_r is the angular velocity of the motor rotor (rad s^{-1}). This expression is analogous to the relationship governing the current through a capacitor

$$I = C\, dv/dt \qquad (17)$$

Hence, the moment of inertia of the motor and fan load may be represented as a capacitor, and the voltage across the capacitor may be used to represent the speed of the motor.

Combining equations (2),(3), and (4) yields

$$\mathbf{i}^T d/dt\, \mathbf{l}_m(\mathbf{q}_r)/w_r = J\, dw_r/dt + B_m\, w_r + w_r^2/K_{fan}^2 \qquad (18)$$

It is thus possible to express (18) as a circuit with the various generated, loss, and load torque expressed as current sources. This circuit is illustrated schematically in Figure 7. The motor speed is obtained by calculating the node voltage labeled w_r in this circuit.
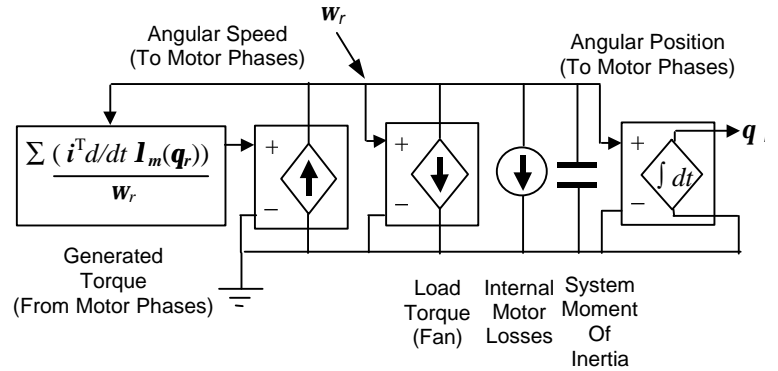

Figure 7. Electromechanical motor model using analog behavioral modeling

The voltage controlled current source used to represent the generated torque is comprised of the sum of the torques generated from each motor phase. The term representing the load torque is a voltage controlled current source incorporating the fan constant for the particular fan load.

The internal motor loss torque, such as bearing friction was modeled as a constant current source. Windage losses in this application were not significant, so they were excluded in the simulation model.

The motor moment of inertia was modeled as a capacitor as implied in equation (17). Finally, the motor speed was integrated by a voltage controlled voltage source to obtain the angular position of the motor rotor. This information was used to determine the phase back EMF and the mutual coupling between phases.

Time Domain Results

Conducted emissions testing to the specification of concern (a CISPR25 variant) was specified at a constant mid speed and constant high speed. As such,

simulations were performed at these speeds and compared with experimentally obtained results.

Although the ultimate goal is to achieve frequency domain data, time domain results provide a qualitative validation of the system model. In comparing simulated and experimental results, the voltages of concern were the positive output of the Line Impedance Stabilization Network (LISN). The results for the 10 turn, 18 AWG motor winding are presented. The simulated positive LISN voltage at medium speed is shown in Figure 7. The measured positive LISN voltage for medium speed conditions is shown in Figure 8.

The comparison between simulated and experimental waveforms is good both in terms of magnitude as well as shape. The maximum positive voltage of the conduction envelope in the simulated case is 66.7 mV which compares well with the measured value of 70.4 mV. The maximum negative voltage of the conduction envelope in the simulated case is –24.9 mV, which also compare well with the measured value of –22.0 mV.
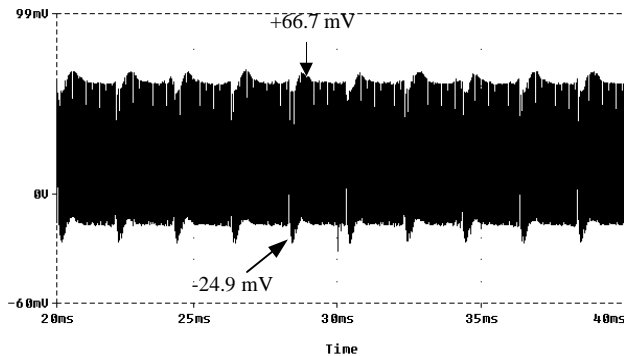

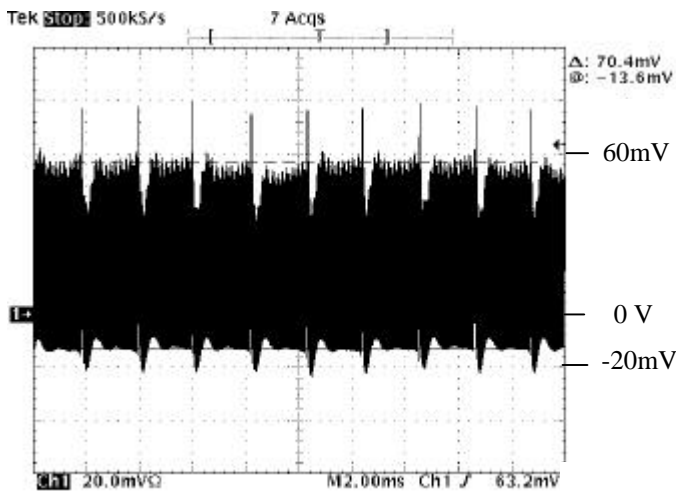**Figure 8. Simulated LISN voltage at mid-speed**

Figure 9. Measured LISN voltage at mid-speed.

The simulated positive LISN voltage at high speed is shown in Figure 9. The measured negative LISN voltage for high speed operation is shown in Figure 10.

Once again, for high speed operation, there is also good comparison between the simulated and measured cases. The large periodic peak in the waveform is the

result of the behaviour of the motor and drive during the transition of one motor phase turning off, to the turning on of the next motor phase in the commutation sequence. In the simulated case, the magnitude of this peak is equal to +63.5 mV, which compares well with the measured value of approximately +62 mV. The maximum negative voltage in the simulated case is equal to –24.6 mV, while in the measured case, the maximum negative voltage is equal to
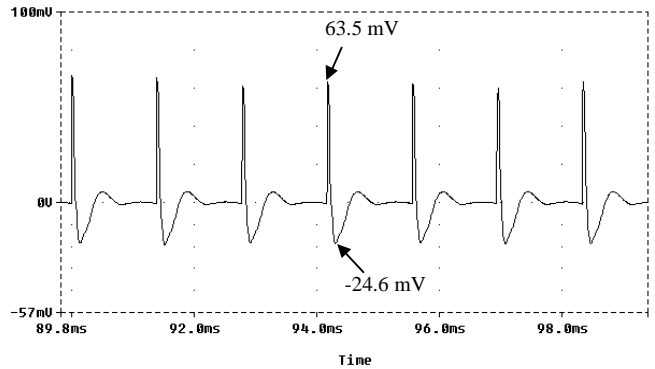–24.8 mV.

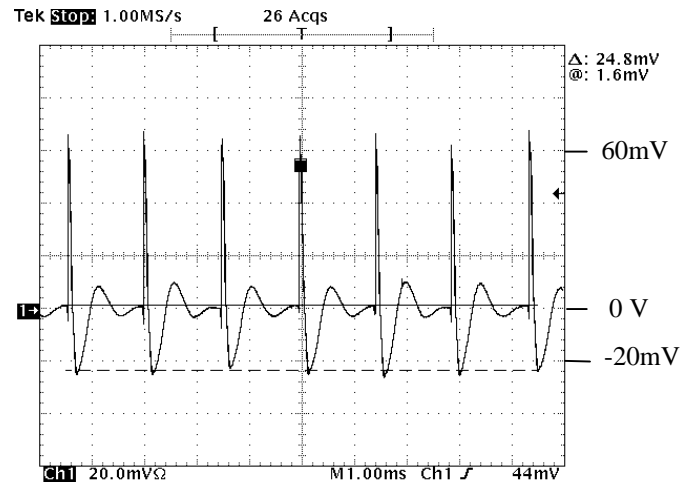**Figure 10. Simulated LISN voltage at high speed.**

Figure 11. Measured LISN voltage at high speed.

Once the time domain LISN voltages were obtained, a method of determining the frequency spectrum of the LISN voltages was implemented.

Determination of Conducted RFI Spectrum

To obtain simulation results that could be correlated directly to measured results, it was decided to simulate the behaviour of a typical superheterodyne spectrum analyzer which might be used in a conducted RFI measurement. The spectrum analyzer parameters that were duplicated in the MATLAB[®] simulation were obtained from a modified version of the CISPR 25 specification. The measurement parameters included an IF bandwidth of 10 kHz, frequency steps of 7.5 kHz, as well as peak detection with no attenuation.

To completely duplicate a superheterodyne type spectrum analyzer in PSPICE® would be impractical due to long computing times. As a result, it was decided to simulate the important features of a spectrum analyzer in MATLAB®.

The method that was adopted, was to pass a sliding window over the time domain data and apply an FFT to the windowed data. The FFT was performed for each window over the entire frequency range of interest at fixed frequency steps. In this case the conducted RFI was calculated every 7.5 kHz from 150 kHz to 1 MHz. To simulate a "peak hold" function of the spectrum analyzer, the FFT values for each window were subsequently compared, and the maximum value of the transform was kept for the particular frequency of interest. The FFT was performed using a rectangular window.

Frequency Domain Results

The FFT results for mid speed operation, and high speed operation for a motor and drive without RFI suppression components appears in Figures 12 and 13 for the 10 turn, 17 AWG motor winding, respectively. The mid speed and high speed results for the 9 turn, 18 AWG winding appear in Figures 14 and 15 respectively. The straight line passing through the data on all graphs is the specification limit for the frequency range of interest. The darker curves on both graphs are the measured results. Table 1 is a summary of the average and worst case errors between simulation and measurement in the medium speed and high speed case for both motor windings.

As may be seen in the results for mid speed operation for the 10 turn, 17 AWG motor winding, the simulated values follow the same trend as the experimental values across the frequency range of interest. The peak measurements obtained in the simulation are higher, however, than the measured case.

The discrepancies are attributable to several factors. The frequency domain data results show better the differences between the measurements and simulations of the LISN voltages. Some discrepancy in the frequency domain magnitudes at low frequencies may be due to the inherent differences between the FFT method used in simulation, and experimental measurement. One discrepancy may have to do with the characteristics of the spectrum analyzer peak detector used in measurement.

In the case of high speed motor operation, the measured and simulated results show a better correlation, with the worst case difference equal to approximately 5.74 dB. In the case of high speed motor operation, the high speed simulation results appear to be more broadband in nature than the experimental results, decreasing at approximately 20 dB per decade.

Considering the 9 turn, 18 AWG motor winding, as may be seen in the results for mid speed operation, the simulated values follow the same trend as the experimental values across the frequency range of interest.

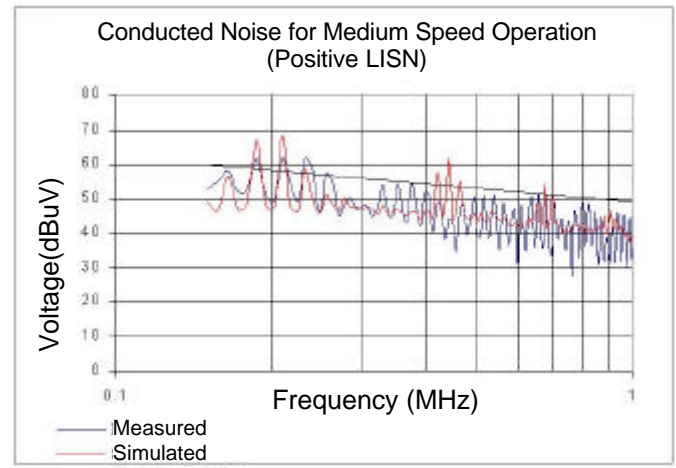The peak measurements obtained in the simulation are higher, however, than the measured case.

Figure 12. Medium speed conducted RFI spectrum (10 turns 17 AWG)

The discrepancies are attributable to several factors. The frequency domain data results show better the differences between the measurements and simulations of the LISN voltages.

Some discrepancy in the frequency domain magnitudes at low frequencies may be due to the inherent differences between the FFT method used in simulation, and experimental measurement. One discrepancy may have to do with the characteristics of the spectrum analyzer peak detector used in measurement.
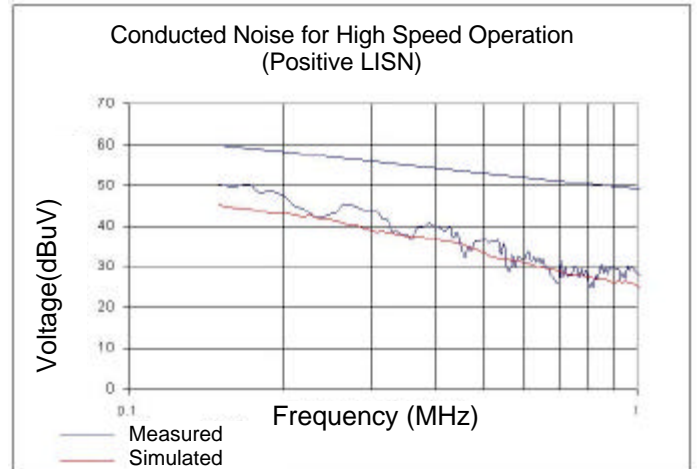

Figure 13. High speed conducted RFI spectrum. (10 turns 17 AWG)

In the case of high speed motor operation, the measured and simulated results show a better correlation, with the worst case difference equal to approximately 5.74 dB. In the case of high speed motor operation, the high speed simulation results appear to be more broadband in nature than the experimental results, decreasing at approximately 20 dB per decade.
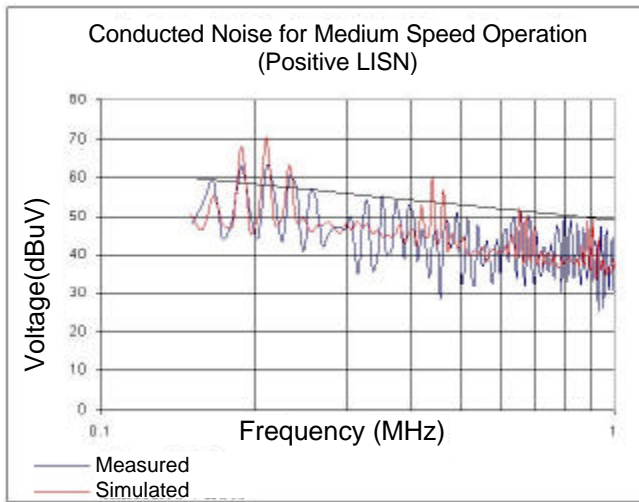
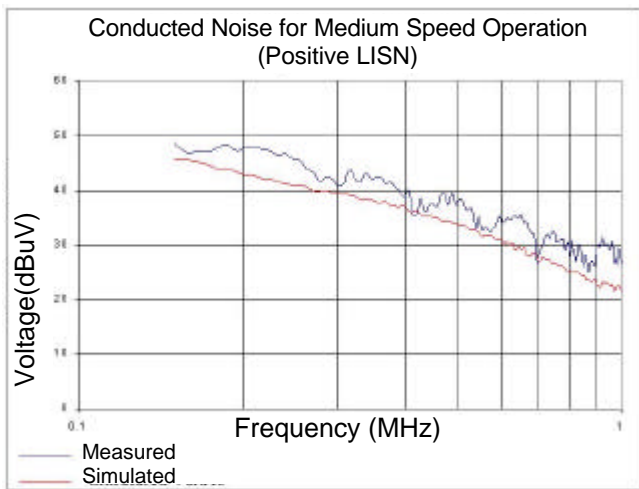**Figure 14. Medium speed conducted RFI spectrum. (9 turns 18 AWG)**

Figure 15. High speed conducted RFI spectrum. (9 turns 18 AWG)

Case Examined	Average Difference (dB)	Worst Case Maximum Difference (dB)	Worst Case Minimum Difference (dB)
Medium Speed (10 T 17 AWG)	-0.85	+9.35 at 0.6825 MHz	-17.47 at 0.4425 MHz
High Speed (10 T 17 AWG)	+1.89	+5.74 at 0.97501 MHz	-3.26 at 0.690001 MHz
Medium Speed (9 T 18 AWG)	-0.347	+11.32 at 0.80251 MHz	-19.068 at 0.93001 MHz
High Speed (9 T 18 AWG)	+3.88	+8.029 at 0.92251 MHz	-1.380 at 0.69751 MHz

Table 2. Summary of error between experimental and simulated conducted RFI spectrum

Conclusions

From the time domain results, one may conclude that using a lumped parameter measured model is an effective method of predicting the time domain LISN voltages from which a conducted RFI spectrum may be obtained.

With respect to frequency domain results, the correlation between simulated and experimental results show a few differences. The simulated results follow the general trend of the experimental results. The discrepancies may be attributable in part, to the methods used to model various motor parameters, and differences between the simulated and experimental methods used to obtain the frequency spectrum.

For example, the phase back EMFs were modeled as the sum of sinusoidal harmonic voltages. In reality, the phase back EMFs are a function of the flux in the air gap. It may be more prudent to use a finite element program to determine the flux in air gap under the load conditions of concern so as to incorporate the effects of armature reaction on the shape of the phase back EMFs. Finite element tools could also be used to predict the values in the self and mutual inductance matrix, as well as iron losses.

In comparing the simulated and experimental results, it can be concluded that this method of predicting conducted RFI emissions over the frequency range of interest can serve as a simulation tool that can shorten the development cycle.

In this study, simulation has only been conducted on two motor windings with two different fan loads. At the present time, to further validate the model the current motor windings with additional RFI suppression components are being evaluated.

References

[1] Zhong, E., Lipo, T.,A., "Improvements in EMC Performance of Inverter-Fed Motor Drives", *IEEE Transactions on Industry Applications*, Vol. 31, No.6, November/December 1995, pp 1247-1256.

[2] Grandi, G., Casadei, D., Reggianni, U., "Analysis of Common- and Differential-Mode HF Current Components in PWM Inverter-Fed AC Motors" , *PESC98, Record of the 29th Annual Power Electronics Specialist Conference*, Fukuoka, Japan, May 17-22, 1998, pp 1146-1151.

[3] Chen., C, Xu, X., "Modeling the Conducted EMI Emission of an Electric Vehicle (EV) Traction Drive", *IEEE 1998 Proceedings on Electromagnetic Compatibility* , pp 796-801.

[4] Ran., L., Gokani., S., Clare., J., "Conducted Electromagnetic Emissions in Induction Motor Drive Systems Part I: Time Domain Analysis and Identification of Dominant Modes", *IEEE Transactions on Power Electronics*, Vol. 13, No. 4, July 1998. pp 757-767.

[5] Ran., L., Gokani., S., Clare., J., "Conducted Electromagnetic Emissions in Induction Motor Drive Systems Part II: Frequency Domain Models", *IEEE Transactions on Power Electronics*, Vol. 13, No. 4, July 1998. pp 768-775.

[6] Zhu, H., Lai, J-S, Hefner, A.R., Tang, Y, Chen, C., "Analysis of Conducted EMI Emissions from PWM Inverter Based on Empirical Models and Comparative Experiments", *Conference Transactions of IEEE Power Electronics Specialist Conference, PESC 99*, pp 861-867.

[7] Spee, R., Wallace., A.K.," Performance Characteristics of Brushless DC Drives", *IEEE Transactions on Industry Applications*, Vol 24, No. 4, July/August 1988, pp 568-573.

[8] Strahan., R.J., "Energy Conversion by Nonlinear Permanent Magnet Machines", *IEE Proc.-Electr. Power Appl.*, Vol. 145, No. 3, May 1998, pp 103-198.

[9] Zhang, J., Mathew, R., Flinders, F., Oghanna, W., "Simulator of DC Traction Motors Including Both Main and Interpole Saturation", *IEE Proc.-Electr. Power Appl.*, Vol. 145, No. 4, July 1998, pp 377-382.

[10] Jack, A.G., Atkinson, D.J., Slater, H.J., "Real-time Emulation for Power Equipment Development. Part 1: Real Time Simulation", *J., IEE Proc.-Electr. Power Appl.*, Vol. 145, No. 2, March 1998, pp 92-97.

[11] Jack, A.G., Atkinson, D.J., Slater, H.J., "Real-time Emulation for Power Equipment Development. Part 2: Real Time Simulation", *J., IEE Proc.-Electr. Power Appl.*, Vol. 145, No. 2, March 1998, pp 153-158.

[12] Cho, D.-H., Kim, K., "Modeling of Electromagnetic Excitation Forces of Small Induction Motor for Vibration and Noise Analysis", *J., IEE Proc.-Electr. Power Appl.*, Vol. 145, No. 3, May 1998, pp 199-205.